Nanofibers with Very Fine Core–Shell Morphology from Anisotropic Micelle of Amphiphilic Crystalline-Coil Block Copolymer

Fei-Yu Zhai,[†] Wei Huang,[†] Gang Wu,[†] Xin-Ke Jing,[†] Mei-Jia Wang,[†] Si-Chong Chen,[†,*] Yu-Zhong Wang,[†] In-Joo Chin,[‡] and Ya Liu[†,*]

[†]Center for Degradable and Flame-Retardant Polymeric Materials (ERCEPM-MoE), National Engineering Laboratory of Eco-Friendly Polymeric Materials (Sichuan), State Key Laboratory of Polymer Materials Engineering, College of Chemistry, Sichuan University, Chengdu 610064, China and [‡]Department of Polymer Science and Engineering, Inha University, Incheon 402-751, Republic of Korea

ABSTRACT A novel and facile strategy, combining anisotropic micellization of amphiphilic crystalline-coil copolymer in water and reassembly during single spinneret electrospinning, was developed for preparing nanofibers with very fine core–shell structure. Polyvinyl alcohol (PVA) and polyethylene glycol-*block*-poly(*p*-dioxanone) (PEG-*b*-PPDO) were used as the shell and the crystallizable core layer, respectively. The core–shell structure could be controllably produced by altering concentration of PEG-*b*-PPDO, and the chain length of the PPDO block. The morphology of the nanofibers was investigated by Transmission Electron Microscope (TEM) and Scanning Electron Microscope (SEM). X-ray rocking curve measurements were performed to investigate the degree of ordered alignment of the PPDO crystalline lamellae in the nanofiber. The results suggested that the morphology of nanoparticles in spinning solution plays very important role in determining the phase separation of nanofibers. The amphiphilic PEG-*b*-PPDO copolymer self-assembled into star anise nanoaggregates in water solution induced by the crystallization of PPDO blocks. When incorporated with PVA, the interaction between PVA and PEG-*b*-PPDO caused a morphological transition of the nanoaggregates from star anise to small flake. For flake-like particles, their flat surface is in favor of compact stacking of PPDO crystalline lamellae and interfusion of amorphous PPDO in the core of nanofibers, leading to a relatively ordered alignment of PPDO crystalline lamellae and well-defined core–shell phase separation. However, for star anise-like nanoaggregates, their multibranched morphology may inevitably prohibit the compact interfusion of PPDO phase, resulting in a random microphase separation.

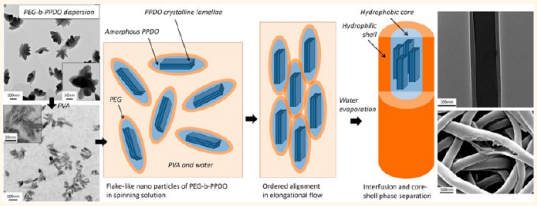

KEYWORDS: single spinneret electrospinning · core–shell nanofiber · crystalline-coil copolymer · anisotropic micelle

Nanofibers with well-defined microstructure, such as core–shell or multilayer coaxial structures, have been the subject of great interest for a number of potential applications because of their diverse properties and functionalities.[1−13] Generally, the core–shell nanofibers can be prepared by coaxial electrospinning.[14−20] Although coaxial electrospinning is attractive as result of simultaneously electrospinning two different polymer solutions into core–shell structured nanofibers, the coaxial electrospinning system has a complicated design requiring two coaxial capillary spinnerets.[14] Single spinneret electrospinning processes, such as emulsion electrospinning,[21,22] blend electrospining[23−33] and template growth[34−38] were also developed for preparing core–shell nanofibers. For the emulsion electrospinning, the immiscibility of core and sheath materials and the stable homogeneous emulsion are crucial to achieve core–shell structures. Blend electrospining is another relatively facile method for preparing core–sheath nanofibers, which is dependent on incompatibility of the polymers, molecular weight of the compositions, and solvent selection. Meanwhile, in many cases, some post-treatment steps are necessary for forming clear phase separation structure.[20,22,27,30,39] Therefore, it still remains a challenge to construct core–shell nanofiber with fine structures by facile and low-cost solution-phase protocols.

Anisotropic nanostructures using crystallization of crystalline-coil copolymer as a main inducing force are especially attractive

* Address correspondence to yya_liu@163.com, chensichong@scu.edu.cn.

Received for review January 7, 2013 and accepted May 7, 2013.

Published online May 07, 2013
10.1021/nn401851w

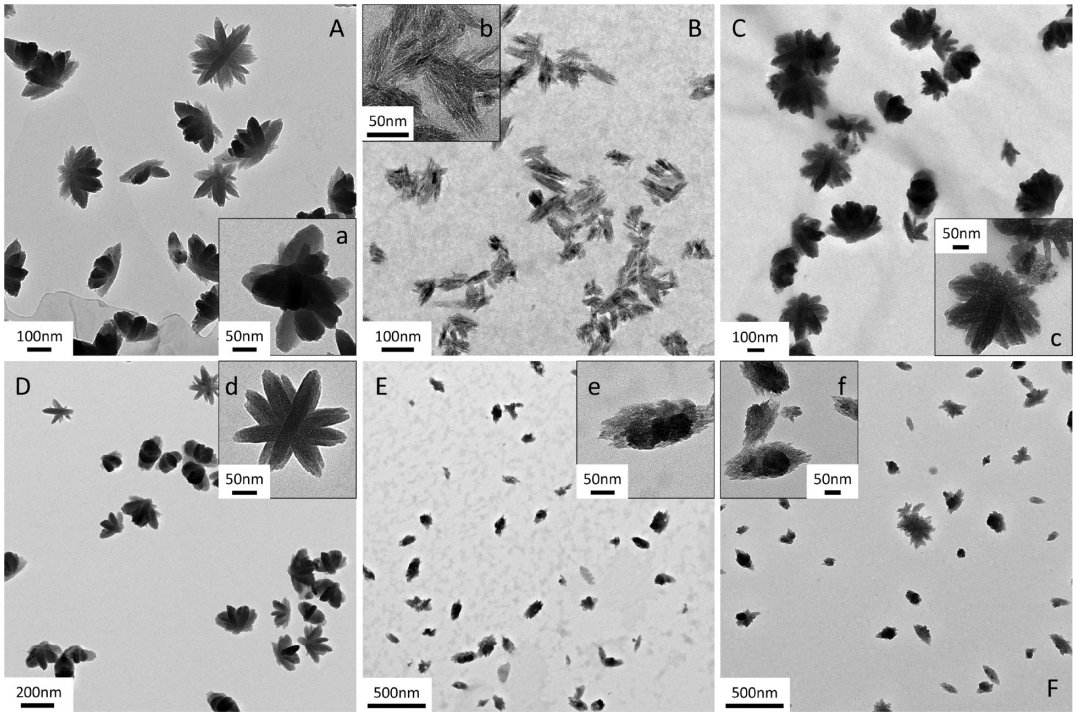

Figure 1. TEM images of $PEG_{45.5}$-*b*-$PPDO_{18}$ (A–C, a–c) and $PEG_{45.5}$-*b*-$PPDO_7$ (D–F, d–f) nanoaggregates in water dispersion (A, a, D, d); with copolymer concentration of 1.6 w/v% (B, b, E, e); in spinning solution, in spinning solution with copolymer concentration of 1.6 w/v% (B, b, E, e); in spinning solution with copolymer concentration of 4.8 w/v% (C, c, F, f). The concentration of PVA in spinning solution is 8 w/v%.

because they can possess complex interparticle interactions useful for the bottom-up design of hierarchical assemblies.[40,41] In our previous works, the TEM images suggested that the amphiphilic crystalline-coil block copolymer based on PPDO, including branched alternating PEG-PPDO multiblock copolymer,[42] mutli-branched PEG-PPDO block copolymer,[43] and PVA-*g*-PPDO graft copolymer,[44] can self-assemble into anisotropic nanoaggregates with star anise-like morphology in water dispersion. The time-dependent self-assembly process of PVA-*g*-PPDO copolymer suggested that the formation of the anisotropic nanoaggregates is a hierarchical assembly process from flake-like particles.[44] At the initial stage, the copolymer formed flake-like particles because the crystallizatioin of PPDO segments may kinetically "trap" this kind of morphology with high interface curvature. With the increase of degree of crystallinity, the flake-like particles tended to interfuse and evolve to the thermodynamically preferred morphology over time. In this work, we developed a novel and facile strategy to produce nanofibers with fine core–shell structure based on the anisotropic nanoparticles of polyethylene glycol-*block*-poly(*p*-dioxanone) (PEG-*b*-PPDO) and single spinneret electrospinning. The PEG-*b*-PPDO diblock copolymers and polyvinyl alcohol (PVA) were used as the core and shell of the nanofiber, respectively.

RESULTS AND DISCUSSION

The PEG-*b*-PPDO diblock copolymer was prepared by using monomethoxy PEG as initiator for ring-opening polymerization of *p*-dioxanone (PDO) (see also in Supporting Information). Two PEG-*b*-PPDO copolymers were used in this work and recorded as PEG*x*-*b*-PPDO*y*, where *x* and *y* represent the degree of polymerization of PEG and PPDO blocks, respectively. The amphiphilic PEG-*b*-PPDO could assemble into anisotropic nanoaggregates with special star anise-like morphology in water (Figure 1A,D). Our previous researches proved that this morphology was induced by the crystallization of PPDO blocks.[42–44]

It was not possible to directly electrospin nanofibers from water dispersion of pure copolymer because the micellization decreased viscosity of the solution obviously. When incorporated with PVA, the spinnability of the PEG-*b*-PPDO solution was improved. The Transmission Electron Microscope (TEM) images of nanoaggregates formed in PVA/$PEG_{45.5}$-*b*-$PPDO_{18}$ spinning solutions with PVA concentration maintaining at 8 w/v% were shown in Figure 1B,C. When copolymer concentration of the spinning solution was 4.8 w/v% (corresponding to the copolymer content of 38 wt % in nanofiber), the nanoparticles formed in spinning solution maintained "star anise"-like morphology. However, when copolymer concentration of the spinning solution was 1.6 w/v% (corresponding to the copolymer content of 17 wt % in nanofiber), the star anise-like aggregates were dissociated into many small pieces with a flake-like morphology. From the TEM image, it can be seen clearly that the flake-like particle was composed of several lamellae (Figure 1b). Meanwhile,

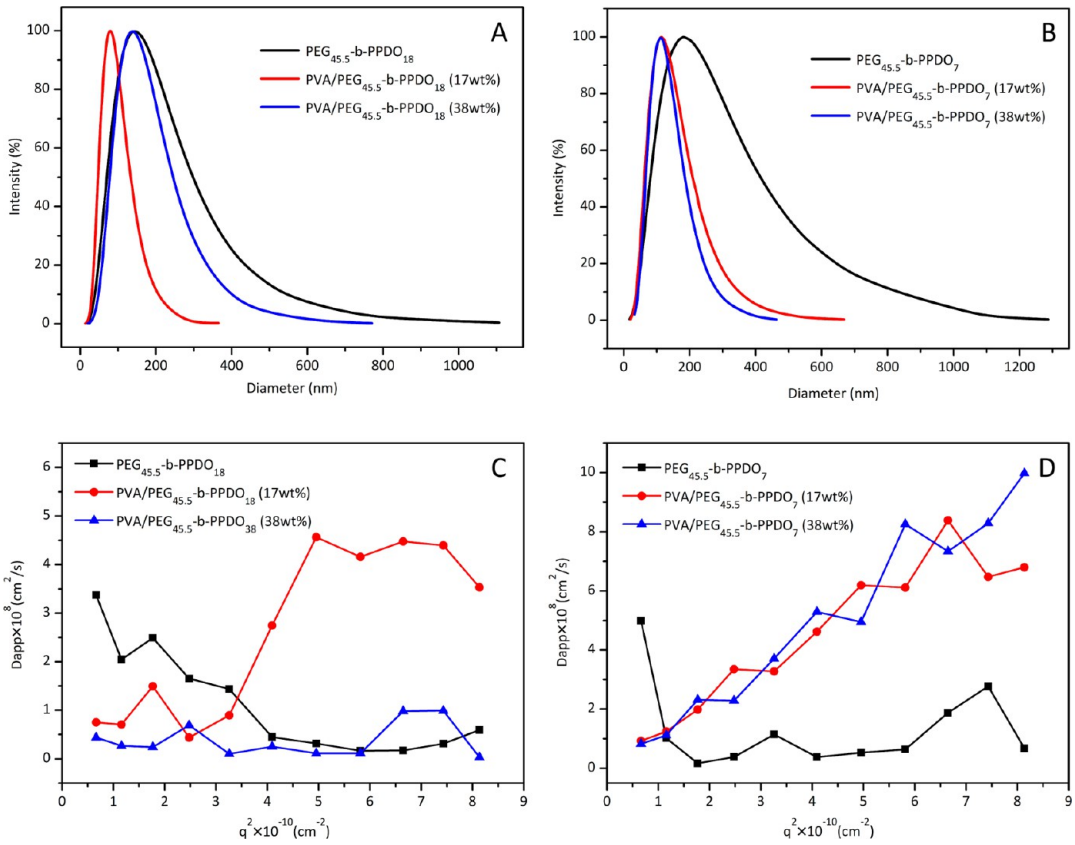

Figure 2. The size distributions of the DLS data and angular dependence (q is the scattering vector) of the apparent diffusion coefficient, Dapp, for nanoparticles of PVA/PEG$_{45.5}$-*b*-PPDO$_{18}$ (A and C), PVA/PEG$_{45.5}$-*b*-PPDO$_7$ (B and D), and the corresponding PEG-*b*-PPDO copolymer.

for PVA/PEG$_{45.5}$-*b*-PPDO$_7$ spinning solutions with copolymer concentration of 1.6 and 4.8 wt/v%, the nanoparticles also showed flake-like morphology in Figure 1E(e) and F(f). Comparing to PVA/PEG$_{45.5}$-*b*-PPDO$_{18}$ (17 wt %), however, the flake-like particles formed by PEG$_{45.5}$-*b*-PPDO$_7$ in spinning solution did not show clear inner structure because of their relatively short PPDO blocks and low crystallinity.

During the formation of star anise-like nanoaggregates, the flake-like particle is a metastable or kinetically "quenched" morphology which evolves to the thermodynamically preferred star anise morphology over time. However, when PVA were added, the hydrophobic−hydrophilic equilibrium of the nanoaggregates was broken. The interaction between hydrophilic PVA and PEG blocks can thermodynamically rather than only kinetically "trap" the flake morphology. This morphological change depends on the mol ratio between PVA and PPDO segments. For example, PVA/PEG$_{45.5}$-*b*-PPDO$_{18}$ (38 wt %) has the highest PPDO content among all samples. The interaction between PVA and PEG blocks of this sample is not strong enough for dissociating the star anise-like nanoparticles (Figure 1C). However, both the outline and inner structure of the nanoparticles became fuzziness owing to the interaction between PVA and PEG. Meanwhile, for those samples with less copolymer content or shorter PPDO blocks than PVA/PEG$_{45.5}$-*b*-PPDO$_{18}$ (38 wt %), the interaction between PVA and PEG blocks overwhelms the cohesion from the hydrophobic semicrystalline PPDO blocks, resulting in a morphological evolution from star anise to flake (Figure 1B,E,F).

The size distributions of the nanoparticles were also recorded by dynamic light scattering (DLS). Figure 2A,B exhibited the size distribution curves of the nanoparticles. DLS results were qualitatively consistent with the assigned change in nanoparticle morphology. The obviously decreased particle size also indicated the dissociation of the star anise like aggregates into flake-like particles.

The angular dependence of the apparent diffusion coefficient (Dapp) *vs* scattering vector (q) is an effective method to determine the anisotropy of the nanoparticles with different morphologies. For spherical particles, Dapp should be independent of the scattering vector because of the undetectable rotational motion.[45,46] As shown in Figure 2C,D, all samples showed angular dependence of the Dapp *vs* q^2 except PVA/PEG$_{45.5}$-*b*-PPDO$_{18}$ (38 wt %). As mentioned above, the nanoparticles of PVA/PEG$_{45.5}$-*b*-PPDO$_{18}$ (38 wt %) maintained star anise-like morphology (Figure 1C). However, owing to the interaction between PVA and

PEG shell of the star anise-like particles, this sample showed a scattering property similar to those of the spherical particles. For PEG-*b*-PPDO dispersion, Dapp decreased with q^2, which could be ascribed to the star anise-like particle morphology. While for those PVA/PEG-*b*-PPDO spinning solutions with flake-like particle morphology, Dapp increased with q^2 related to the formation of nonspherical aggregates with an elongated shape. Although both star anise-like and flake-like particles are anisotropic, they exhibited different angular dependence of the Dapp *vs.* scattering vector because of their much different anisotropy. The difference in angular dependence also confirmed the evolution in particle morphology after PVA was added in the spinning solution.

The viscosities of samples were recorded by a rotational viscometer. According to the scaling theory of Tawari,[47] the higher concentration of polymer solution possessed, the larger viscosity would be exhibited. As listed in Table 1, however, the viscosity of PVA/PEG-*b*-PPDO spinning solutions with copolymer content of 17 wt % was obviously lower than neat PVA solutions with same PVA concentration. The viscosity gradually increased when more copolymers were added. For $PEG_{45.5}$-*b*-$PPDO_{18}$ (30 wt %) and $PEG_{45.5}$-*b*-$PPDO_{18}$ (38 wt %), they showed even higher viscosity than that of neat PVA. This phenomenon suggested that the morphology of nanoparticle have very important influence on the chain entanglement of PVA in the spinning solution.

The rheological behavior of the PVA/PEG-*b*-PPDO and neat PVA spinning solutions was also investigated by a dynamic rheometer on the concentration range in order to identify the different concentration regimes in which polymer chain entanglements dominate the flow behavior.[48−50] As shown in Figure 3, the spinning solutions of PVA/$PEG_{45.5}$-*b*-$PPDO_{18}$ (17 wt %) exhibited obvious shear thinning behavior, comparing to neat PVA and PVA/$PEG_{45.5}$-*b*-$PPDO_{18}$ with high copolymer content. Meanwhile, The PVA/$PEG_{45.5}$-*b*-$PPDO_{18}$ (30 wt %) and PVA/$PEG_{45.5}$-*b*-$PPDO_{18}$ (38 wt %) showed higher viscosities than neat PVA and PVA/$PEG_{45.5}$-*b*-$PPDO_{18}$ (17 wt %). The flake-like nanoparticles in PVA/$PEG_{45.5}$-*b*-$PPDO_{18}$ (17 wt %) solution have much better orientation property than that of star anise-like aggregates during shearing, leading to low internal friction and high orientation of the chains.[50−52] While for star anise-like aggregates, their multibranched morphology is in favor of chain entanglements of PVA. Therefore, the spinning solutions of PVA/$PEG_{45.5}$-*b*-$PPDO_{18}$ with high copolymer content show higher viscosities than neat PVA.

The interaction between PVA and PEG could also enhance the stability of the copolymer nanoaggregates. For example, the dispersion of $PEG_{45.5}$-*b*-$PPDO_{18}$ nanoaggregates without PVA could only maintain stable when the copolymer concentration was 1.6 wt/v% or lower. However, the spinning solution of PVA/$PEG_{45.5}$-*b*-$PPDO_{18}$ showed very good stability even at high copolymer concentration.

TABLE 1. The Viscosities of the PVA/PEG-*b*-PPDO Spinning Solutions with Different Copolymer Concentrations

sample	$C_{PEG\text{-}b\text{-}PPDO}$ (w/v%)[a]	PEG-*b*-PPDO content in nanofiber (wt %)	viscosity (Pa/s)
PVA	0	0	1.12
PVA/$PEG_{45.5}$-*b*-$PPDO_{18}$ (17 wt %)	1.6	17	0.87
PVA/$PEG_{45.5}$-*b*-$PPDO_{18}$ (30 wt %)	3.2	30	1.38
PVA/$PEG_{45.5}$-*b*-$PPDO_{18}$ (38 wt %)	4.8	38	1.70
PVA/$PEG_{45.5}$-*b*-$PPDO_7$ (17 wt %)	1.6	17	0.95
PVA/$PEG_{45.5}$-*b*-$PPDO_7$ (30 wt %)	3.2	30	1.02
PVA/$PEG_{45.5}$-*b*-$PPDO_7$ (38 wt %)	4.8	38	1.04

[a] $C_{PEG\text{-}b\text{-}PPDO}$ are concentrations of the PEG-*b*-PPDO in the spinning solution; the PVA concentration of all samples is 8 w/v%.

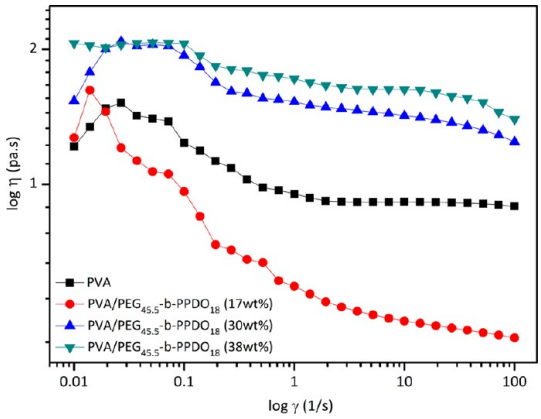

Figure 3. Logarithmic plot of viscosity as a function of shear rate of PVA and PVA/$PEG_{45.5}$-*b*-$PPDO_{18}$ with different copolymer concentrations.

All samples can be electrospun into uniform nanofibers with smooth surface and diameter range of 100−200 nm. Figure 4A−C present the TEM images of electrospun of PVA/$PEG_{45.5}$-*b*-$PPDO_{18}$ with different copolymer weight content (17, 30, and 38 wt %, respectively). It is notable that only the PVA/$PEG_{45.5}$-*b*-$PPDO_{18}$ (17 wt %) can form clear core−shell morphology. Since no stain was used in TEM test for nanofiber, while the copolymer have relatively much higher crystallinity than PVA, the dark regions of the nanofibers are identified as the semicrystallized PPDO phase. With the increase of copolymer content, no obvious core−shell phase-separation structures was obtained and the boundary between PVA and PEG-*b*-PPDO was less evident (Figure 4B,C).

To indentify the core−shell morphology of the nanofibers, the electrospun membranes of PVA/$PEG_{45.5}$-*b*-$PPDO_{18}$ were soaked in $CHCl_3$ for selectively removing the PEG-*b*-PPDO since the $CHCl_3$ is good solvent for PEG-*b*-PPDO but poor solvent for PVA. The phase separation between PVA and PEG-*b*-PPDO in the nanofiber could therefore be observed by Scanning Electron Microscope (SEM). The SEM images of the

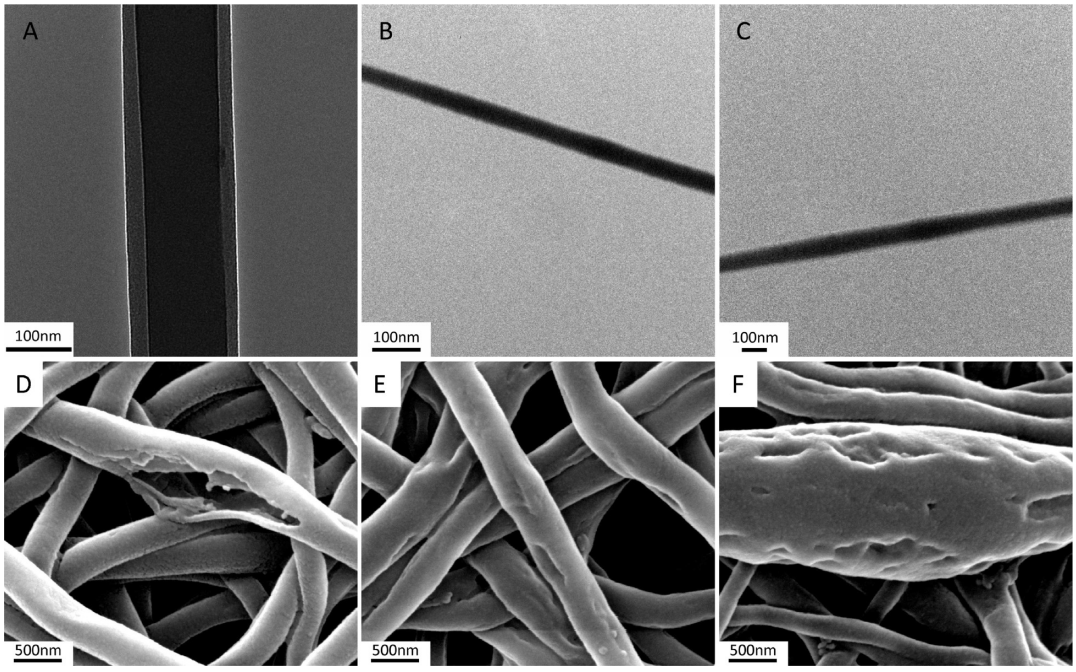

Figure 4. TEM (A–C) images of the electrospun nanofibers of PVA/PEG$_{45.5}$-*b*-PPDO$_{18}$ with different copolymer content and SEM images (D–F) of corresponding nanofibers after selectively removing of the copolymer. The weight contents of copolymer are 17 wt % (A and D), 30 wt % (B and E) and 38 wt % (C and F), respectively.

nanofibers after selectively removing the PEG-*b*-PPDO are presented in Figure 4D–F. It is clear to see that the surface of the nanofiber with 17 wt % of copolymer did not show obvious change after the extraction. However, we also found a very few sections of the nanofibers were broken because of the extraction (Figure 4D). Hollow internal structure could be observed in these broken segments which confirmed the core–shell phase separation of the nanofibers, and the PEG-*b*-PPDO served as core while PVA served as shell of the nanofibers, respectively. For PVA/PEG$_{45.5}$-*b*-PPDO$_{18}$ with high copolymer content (30 and 38 wt %), the surface of the nanofibers became rough and accidented (Figure 4E,F) while no hollow internal structure was observed. These results suggested the absence of core–shell structure and were in accordance with TEM observation. The mass losses of the PVA/PEG$_{45.5}$-*b*-PPDO$_{18}$ samples, calculated by weighting the samples before and after selectively removing PEG-*b*-PPDO, are 16.1, 28.2, and 36.9 wt %, respectively, and very close to the theoretical values.

Fourier Transform Infrared Spectroscopy (FT-IR) reflectance spectrum of the PVA/PEG$_{45.5}$-*b*-PPDO$_{18}$ nanofibers, neat PVA nanofiber and PEG$_{45.5}$-*b*-PPDO$_{18}$ powder were presented in Figure 5. The neat PVA nanofibers exhibited a broad absorption peak at 3419 cm^{-1} and weak absorption peaks at 1639 and 1106 cm^{-1}, which were attributed to the O–H stretching of the hydroxyl groups, H–OH bend, and C–O stretching, respectively. Meanwhile, PEG-*b*-PPDO powder showed characteristic peaks at 2906, 1731, 1220, and 1134 cm^{-1} corresponding to the C–H stretching,

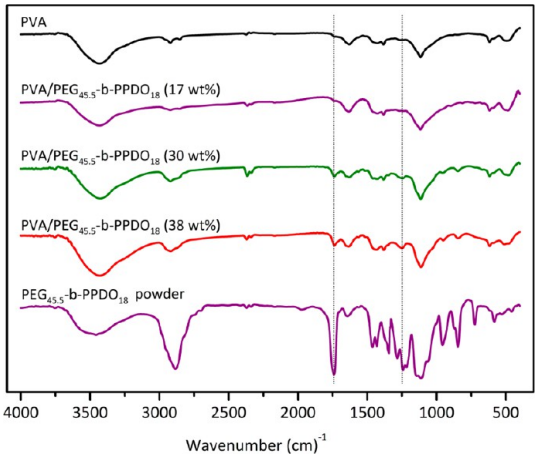

Figure 5. The FT-IR reflectance spectra of the PVA/PEG$_{45.5}$-*b*-PPDO$_{18}$ electrospun nanofibers, neat PVA nanofibers and PEG$_{45.5}$-*b*-PPDO$_{18}$ powder.

C=O stretching, C–O–C, and C–O stretching, respectively. When PEG-*b*-PPDO content was 17 wt %, the spectrum of the nanofiber was very similar to that of PVA because of the fine core–shell morphology of this sample. However, for other two samples with higher PEG-*b*-PPDO content, characteristic peaks of PPDO block could be observed at 1731 and 1220 cm^{-1}, suggesting that the copolymer distributed not only in the inner part, but also on the surface of the nanofibers owing to the absence of core–shell structure of these samples.

Different from PVA/PEG$_{45.5}$-*b*-PPDO$_{18}$, fine core–shell structure was observed for all three samples of PVA/PEG$_{45.5}$-*b*-PPDO$_{7}$ (Figure 6). Interestingly,

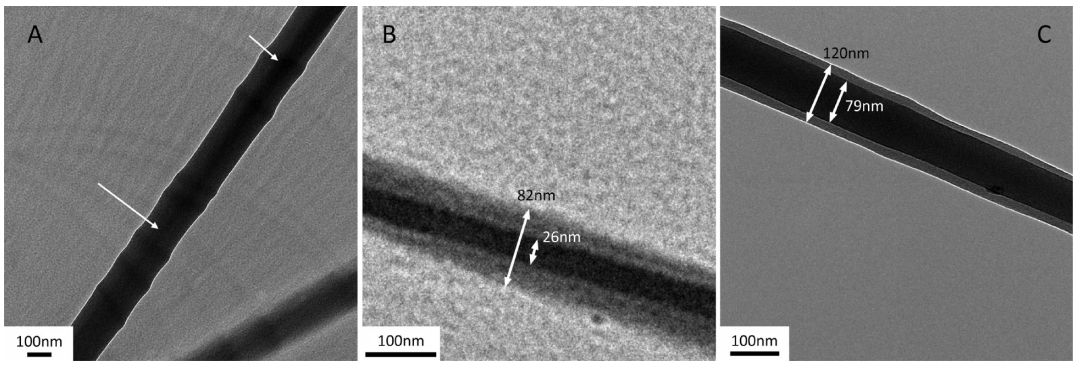

Figure 6. TEM images of the PVA/PEG$_{45.5}$-*b*-PPDO$_7$ electrospun nanofibers with different PEG$_{45.5}$-*b*-PPDO$_7$ contents, (A) 17 wt %, (B) 30 wt %, (C) 38 wt %, respectively.

PVA/PEG$_{45.5}$-*b*-PPDO$_7$ nanofibers with 17 wt % of copolymer content showed a discontinuous core–shell structure as marked by white arrows in Figure 6A. This phenomenon could be attributed to the molecular structure of the copolymer. Since the PPDO block of PEG$_{45.5}$-*b*-PPDO$_7$ is much shorter than that of PEG$_{45.5}$-*b*-PPDO$_{18}$, the weight fraction and crystallinity of PPDO block of this sample are not high enough for forming continuous core. Comparatively, the PVA/PEG$_{45.5}$-*b*-PPDO$_7$ nanofibers with high copolymer content (30 and 38 wt %) showed very uniform core–shell structure with obvious boundary (Figure 6B,C). Moreover, the diameter of the core increased with the copolymer content.

Similar to the PVA/PEG$_{45.5}$-*b*-PPDO$_{18}$ (17 wt %), PEG$_{45.5}$-*b*-PPDO$_7$ can form flake-like particles in spinning solution even at high copolymer content (38 wt %, Figure 1F) because of its relatively short PPDO blocks. Meanwhile, the nanofibers of PVA/PEG$_{45.5}$-*b*-PPDO$_7$ samples also exhibited similar core–shell phase separation to PVA/PEG$_{45.5}$-*b*-PPDO$_{18}$ (17 wt %). This phenomenon suggested that the morphology of nanoparticles in spinning solution plays very important role in determining the phase separation of nanofibers.

X-ray rocking curve measurements were performed to investigate the degree of ordered alignment of the PPDO crystalline lamellae in the nanofiber. The rocking curve was recorded by the so-called-ω scan wherein the detector remains fixed at the required 2θ of the plane of interest (usually the plane with the same hkl out-of-plane direction) and the sample is rotated near the Bragg condition. Here the diffraction scan is through the Bragg spot along an orientation orthogonal to the nanofibers growth direction.[53−55] In the ω-rocking curve, the full width at half-maximum (fwhm) of selected diffraction peak provides a direct measure of the angular distribution of textures around the normal direction to the substrate corresponding to orientational distribution of PPDO crystalline lamellae.[54,55] Changes in scattered intensity at a locked direction of the scattering vectors correspond to the distribution of orientation of the diffracted lattice plane.[54] Increases of fwhm and reduction of scattered intensity indicate the enhancement of misorientation.[54−58] In the contrary, narrow fwhm of diffraction peak and high scattered intensity indicate strong orientation.[55−59]

Figure 7A,B showed the WXRD spectra of PVA/PEG$_{45.5}$-*b*-PPDO$_{18}$ and PVA/PEG$_{45.5}$-b*b*-PPDO$_7$ nanofibers with different copolymer contents, respectively. The diffraction peak at $2\theta = 21.98°$ is the major diffraction peak of PPDO blocks corresponding to (210) lattice plane reflection.[60] The ω-rocking curves of the (210) PPDO reflection of different samples were shown in Figure 7C,D. The diffraction peaks of nanofibers with core–shell phase separation (PVA/PEG$_{45.5}$-*b*-PPDO$_{18}$ (17 wt %) and all three PVA/PEG$_{45.5}$-*b*-PPDO$_7$ samples) exhibited a obvious dependence of intensity *vs* ω. Such dependence was not observed for those nanofibers with microphase separation, whose intensity of diffraction peak did not show obvious change with ω (red and blue lines, Figure 7C). The fwhm of diffraction peaks of nanofibers with core–shell morphology were also obviously smaller (around 11°) than the latter (around 16°). Moreover, the nanofibers with core–shell morphology also showed relatively high scattered intensity of diffraction peaks. These results indicated that the PPDO crystalline lamellae in nanofibers with core–shell morphology have much more ordered alignment in the radial direction than those in nanofibers with microphase separation. Stacking layer by layer of the flake-like nanoparticles in the core is a possible explanation for the ordered alignment of PPDO crystalline lamellae, as shown in Figure 7E.

A hypothetical mechanism about the formation of PVA/PEG-*b*-PPDO core–shell nanofibers is proposed as follows (Figure 8). The amphiphilic PEG-*b*-PPDO copolymer self-assembled into star anise nanoaggregates in water solution induced by the crystallization of PPDO blocks. When incorporated with PVA, the interaction between PVA and PEG-*b*-PPDO may cause a morphological transition of the nanoaggregates from star anise to small flake. Greenfeld *et al.* proposed a mechanism for the formation of the internal nanostructure of electrospun polymer nanofibers.[61,62] The suggested

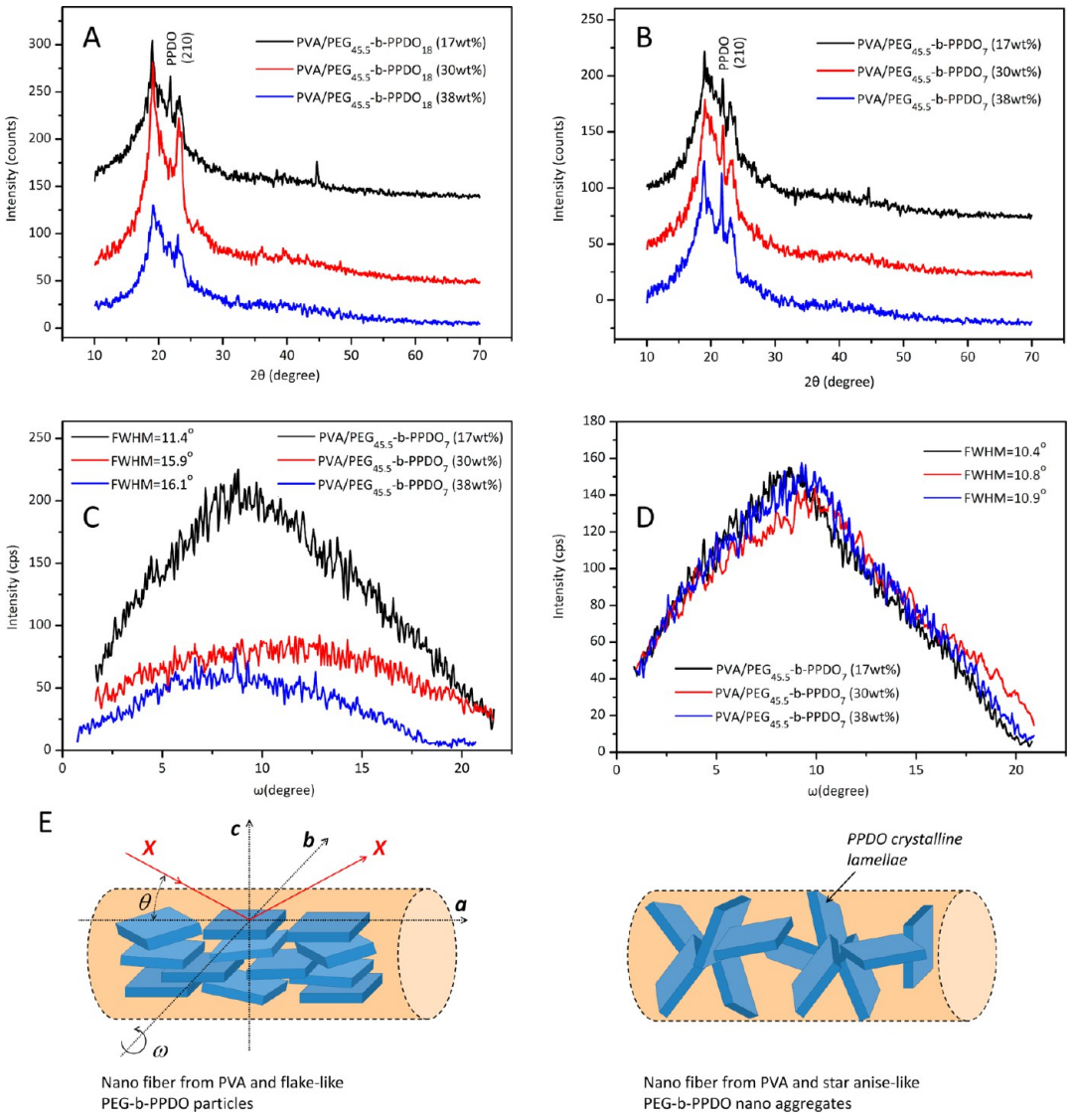

Figure 7. WXRD patterns of PVA/PEG$_{45.5}$-*b*-PPDO$_{18}$ nanofibers (A) and PVA/PEG$_{45.5}$-*b*-PPDO$_7$ nanofibers (B) with different copolymer content, respectively; rocking curves of (210, 2θ = 21.98) PPDO reflection in PVA/PEG$_{45.5}$-*b*-PPDO$_{18}$ (C) and PVA/PEG$_{45.5}$-*b*-PPDO$_7$ (D) nanofibers, respectively; schematic description of distribution of the PPDO crystalline lamellae in the nanofiber (E).

model is based on the polymer solution elongational dynamics which describes a fast axial stretching and orientation of the polymer network accompanied by radial contraction toward the core. This results in a higher polymer concentration and orientation at the fiber center. The suggested model also predicts the presence of an internal spatial variation of the polymer density and molecular orientation. When amphiphilic nanoparticles exist in the spinning solution, as in this work, the radial contraction of the hydrophilic PVA polymer network is accompanied by expelling of the hydrophobic PPDO crystals to the core area of the fibers because the solvent is water. For flake-like particles, their flat surface is in favor of particles stacking layer by layer, leading to a relatively ordered and anisotropic alignment of PPDO crystalline lamellae in radial direction. With the gradually evaporation of water, the semicrystallized hydrophobic PPDO phase tend to merge together to decrease the interfacial energy between hydrophobic phase and hydrophilic phase. However, for star anise-like nanoaggregates, their multibranched morphology may inevitably prohibit the compact aggregation of PPDO phase. Moreover, the multibranched star anise-like morphology may also gradually increase the entanglements of PVA chains as the water evaporating, and impede the phase separation.[63] Therefore, most of star anise-like nanoparticles do not have sufficient mobility and time to reassemble into equilibrium morphology, and microphase separation rather than core−shell morphology was obtained.

CONCLUSIONS

To summarize, we have developed a novel and facile strategy for preparing nanofiber with very fine

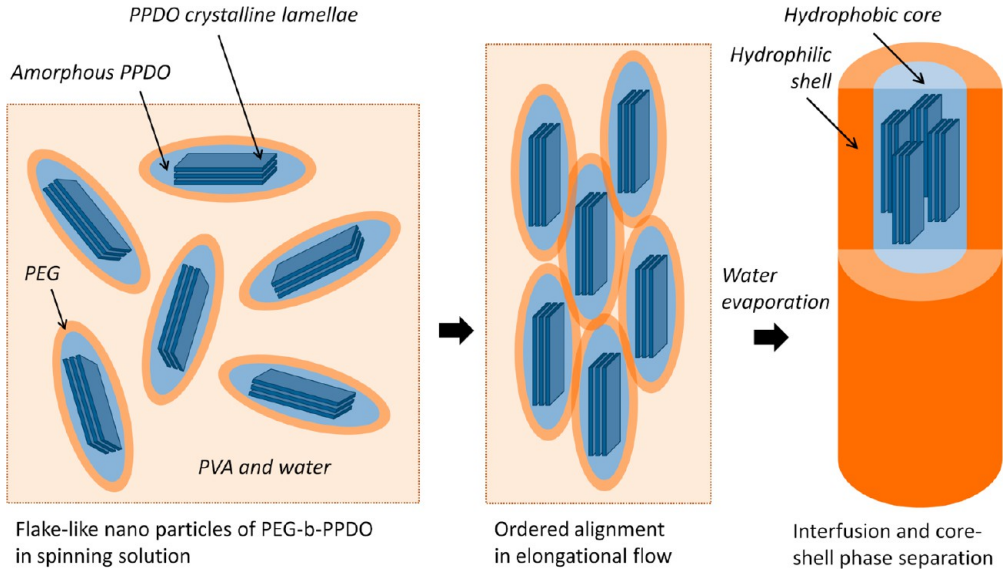

Figure 8. Hypothetical formation mechanism of PVA/PEG-*b*-PPDO core−shell nanofibers.

core−shell morphology *via* single spinneret electrospinning. Owing to the crystallization of hydrophobic PPDO segment, the copolymer formed anisotropic flake-like particles in spinning solution with PVA using water as solvent. The spinning solution was then directly electrospun into nanofibers with hydrophilic shell and hydrophobic semicrystalline core. The core−shell structure of the nanofiber could be controlled by the molecular structure and the concentration of the copolymer. The morphology of the nanoparticles and their interaction with PVA in spinning solution played important roles in determining the phase separation of nanofibers. This novel and facile strategy will allow access to a wide variety of multifunctional nanofibers with well-defined core−shell morphology.

EXPERIMENTAL METHODS

Materials. PVA (degree of polymerization 1700, degree of hydrolysis 88%) was purchased from Alfa Aesar and was used after dried under vacuum at 40 °C until constant weight. PDO (99.9%) with a melt point of 25 °C was provided by the Pilot Plant of the Center for Degradable and Flame-Retardant Polymeric Materials (Chengdu, China), and dried over CaH_2 for 48 h and then distilled under a reduced pressure of 70 Pa just before use. Stannous octoate ($SnOct_2$) (95%) was purchased from Sigma, and was stored in glass ampules under argon after diluted with anhydrous toluene. Two different compositions of polyethylene glycol-*block*-poly(*p*-dioxanone) (PEG-*b*-PPDO) diblock copolymers were synthesized (Supporting Information Scheme S1) and used for electrospinning.

Spinning Solutions. A certain amount of PVA powder was dissolved in distilled water at 70 °C for 12 h and then cooled to 30 °C to prepare PVA solution. The dispersion of copolymer was then dropped into PVA solution under stirring for 12 h to obtain homogeneous aqueous solutions, and the weight content of PEG-*b*-PPDO was controlled at 17, 30, and 38 wt %. After diluting to certain volume, the final concentration of PVA was kept at 8 wt %. The prepared solution was left to rest for 2−3 h for degassing and kept in sealed containers at room temperature. Prior to electrospinning, the as-prepared solutions were measured for their viscosity using a rotational viscometer (NDJ-1, Shanghai, China)

Electrospinning. In the electrosinning unit (SS-2534H, Ucalery, Bei Jing, China), the PVA/PEG-*b*-PPDO spinning solution was placed in a 10 mL syringe, which was mounted in a syringe pump. The polymer solution was fed through the needle tip using a syringe pump at 0.3 mm/min flow rate. A grounded metal mesh screen was placed vertically under the needle tip. A positive high-voltage supply was used to maintain the voltage in the range of 12−20 kV, and the distance between the needle tip and the grid was 22 cm.

Selective Extraction of Electrospun Membranes. Electrospun membranes prepared from corresponding solutions were dried in vacuo at 40 °C for 14 h, and cut into specific dimensions of 3 cm × 3 cm. The samples were accurately weighed in an electronic balance before and after immersion in $CHCl_3$ for 6 h at 90 °C. After the samples were taken out of $CHCl_3$ and dried, the samples were weighted again. After the selective extraction in $CHCl_3$, the eletrospun membranes were evaluated by SEM. The following equation was used to calculate the mass loss of the electrospun membranes.

$$\text{Massloss}\ (\%) = (m_a - m_b)/m_a \times 100\% \qquad (1)$$

Where m_a and m_b were the masses of the membrane before and after the extraction in the $CHCl_3$, respectively.

Morphology. Surface morphology of nanofibers was examined by Scanning Electron Microscopy (SEM) (JSM-5900LV, JEOL Co. Japan) operated at 20 kV. The samples were observed at magnifications 20000 times of their original size. The inner morphology of the nanofiber was observed by Transmission Electron Microscope (TEM, Tecnai G2 F20 S-TWIN electron microscope (FEI Co.)) operated at an acceleration voltage of 200 kV. In the TEM study, nanofibers were collected on a copper specimen grid without staining. TEM images of nanoparticles of PVA/PEG-*b*-PPDO and PEG-*b*-PPDO assembled in aqueous solution were also recorded after staining by 2% OsO_4 solution for 10 min.

Fourier Transform Infrared Spectroscopy. FT-IR (Nicolet G200) spectra was recorded for pure PVA nanofibers, PEG-*b*-PPDO powder and PVA/PEG-*b*-PPDO nanofibers in attenuated total reflection (ATR) mode using an IR spectrophotometer at wavelengths in the range of 500−4000 cm^{-1}.

X-ray Diffraction Measurements. XRD measurements were recorded on a PANALYTITAL X′pert X-ray diffractometer. X-ray diffraction rocking curves were carried out to identify the crystal orientation of the PPDO in PVA/PEG-*b*-PPDO nanofibers.

For rocking-curve scan, the scanning speed was 10°/min, and the angular interval between steps was 0.1°. Rocking curves of the (210) PPDO reflections were measured.

Dynamic Light Scattering. DLS measurements were performed on a Brookhaven model BI-200SM spectrometer and 9000AT correlator using a Innova304 He−Ne laser (1 W, λ = 532 nm). Multiangles scattering experiments were performed at scattering angles θ from 30° to 130° with an interval of 10°. At each angle, the acquisition time and temperature were set to be 1 min and 25 °C, respectively. The samples were last dissolved in water at a concentration of 0.4 mg/mL, which is a good solvent for PEG blocks.

Rheological Measurements. The rheological properties of the PVA/PEG-*b*-PPDO solutions were determined on a AR-2000, TA Instruments, New Castle, DE. The measuring system presents cone−plate geometry with a cone angle of 4° and a diameter of 40 mm. Shear viscosities were registered over the 0.01−100 s^{-1} shear rate domain for surprising all possible flow regimes, at the room temperatures.

Conflict of Interest: The authors declare no competing financial interest.

Supporting Information Available: Synthesis of PEG-*b*-PPDO, SEM images and DSC analysis of the nanofibers. This material is available free of charge *via* the Internet at http://pubs.acs.org.

Acknowledgment. This work was financially supported by the National Natural Science Foundation of China (No. 21274093 and No. 51121001), Program of International S&T Cooperation (2011DFA51420). The Analytical and Testing Center of Sichuan University provided TEM analysis.

REFERENCES AND NOTES

1. Sun, Z. C.; Zussman, E.; Yarin, A. L.; Wendorff, J. H.; Greiner, A. Compound Core-Shell Polymer Nanofibers by Co-Electrospinning. *Adv. Mater.* **2003**, *15*, 1929–1932.
2. Xie, Y.; Qiao, Z. P.; Chen, M.; Liu, X. M.; Qian, Y. T. γ-Irradiation Route to Semiconductor/Polymer Nanocable Fabrication. *Adv. Mater.* **1999**, *11*, 1512–1515.
3. Morales, A. M.; Lieber, C. M. A Laser Ablation Method for the Synthesis of Crystalline Semiconductor Nanowires. *Science* **1998**, *279*, 208–211.
4. Suenaga, K.; Colliex, C.; Demoncy, N.; Loiseau, A.; Pascard, H.; Willaime, F. Synthesis of Nanoparticles and Nanotubes with Well-Separated Layers of Boron Nitride and Carbon. *Science* **1997**, *278*, 653–655.
5. Wei, M.; Kang, B. W.; Sung, C. M.; Mead, J. Core-Sheath Structure in Electrospun Nanofibers from Polymer Blends. *Macromol. Mater. Eng.* **2006**, *291*, 1307–1314.
6. Lauhon, L. J.; Gudiksen, M. S.; Wang, C. L.; Lieber, C. M. Epitaxial Core-Shell and Core-Multishell Nanowire Heterostructures. *Nature* **2002**, *420*, 57–61.
7. Langer, R.; Vacanti, J. P. Tissue Engineering. *Science* **1993**, *260*, 920–6.
8. Koh, C. J.; Atala, A. Tissue Engineering, Stem Cells, and Cloning: Opportunities for Regenerative Medicine. *J. Am. Soc. Nephrol.* **2004**, *15*, 1113–1125.
9. Li, D.; Xia, Y. N. Direct Fabrication of Composite and Ceramic Hollow Nanofibers by Electrospinning. *Nano Lett.* **2004**, *4*, 933–938.
10. Wang, X. Y.; Drew, C.; Lee, S. H.; Senecal, K. J.; Kumar, J.; Sarnuelson, L. A. Electrospun Nanofibrous Membranes for Highly Sensitive Optical Sensors. *Nano Lett.* **2002**, *2*, 1273–1275.
11. Huang, J. S.; Hou, H. Q.; You, T. Y. Highly Efficient Electrocatalytic Oxidation of Formic Acid by Electrospun Carbon Nanofiber-Supported PtxAu100-x Bimetallic Electrocatalyst. *Electrochem. Commun.* **2009**, *11*, 1281–1284.
12. Agarwal, S.; Wendorff, J. H.; Greiner, A. Use of Electrospinning Technique for Biomedical Applications. *Polymer* **2008**, *49*, 5603–5621.
13. Hong, Y. L.; Chen, X. S.; Jing, X. B.; Fan, H. S.; Gu, Z. W.; Zhang, X. D. Fabrication and Drug Delivery of Ultrathin Mesoporous Bioactive Glass Hollow Fibers. *Adv. Funct. Mater.* **2010**, *20*, 1503–1510.
14. Kalra, V.; Lee, J. H.; Park, J. H.; Marquez, M.; Joo, Y. L. Confined Assembly of Asymmetric Block-Copolymer Nanofibers *via* Multiaxial Jet Electrospinning. *Small* **2009**, *5*, 2323–2332.
15. Pakravan, M.; Heuzey, M. C.; Ajji, A. Core-Shell Structured PEO-Chitosan Nanofibers by Coaxial Electrospinning. *Biomacromolecules* **2012**, *13*, 412–421.
16. Ma, M. L.; Krikorian, V.; Yu, J. H.; Thomas, E. L.; Rutledge, G. C. Electrospun Polymer Nanofibers with Internal Periodic Structure Obtained by Microphase Separation of Cylindrically Confined Block Copolymers. *Nano Lett.* **2006**, *6*, 2969–2972.
17. Yang, H.; Lightner, C. R.; Dong, L. Light-Emitting Coaxial Nanofibers. *ACS Nano* **2011**, *6*, 622–628.
18. Kalra, V.; Mendez, S.; Lee, J. H.; Nguyen, H.; Marquez, M.; Joo, Y. L. Confined Assembly in Coaxially Electrospun Block-Copolymer Fibers. *Adv. Mater.* **2006**, *18*, 3299–3303.
19. Hwang, T. H.; Lee, Y. M.; Kong, B. S.; Seo, J. S.; Choi, J. W. Electrospun Core-Shell Fibers for Robust Silicon Nanoparticle-Based Lithium Ion Battery Anodes. *Nano Lett.* **2011**, *12*, 802–807.
20. Yi, F.; Lavan, D. A. Poly(glycerol sebacate) Nanofiber Scaffolds by Core/Shell Electrospinning. *Macromol. Biosci.* **2008**, *8*, 803–806.
21. Xu, X. L.; Zhuang, X. L.; Chen, X. S.; Wang, X. R.; Yang, L. X.; Jing, X. B. Preparation of Core-Sheath Composite Nanofibers by Emulsion Electrospinning. *Macromol. Rapid Commun.* **2006**, *27*, 1637–1642.
22. Yarin, A. L. Coaxial Electrospinning and Emulsion Electrospinning of Core-Shell Fibers. *Polym. Adv. Technol.* **2011**, *22*, 310–317.
23. Gentsch, R.; Pippig, F.; Schmidt, S.; Cernoch, P.; Polleux, J.; Borner, H. G. Single-Step Electrospinning to Bioactive Polymer Nanofibers. *Macromolecules* **2011**, *44*, 453–461.
24. Valiquette, D.; Pellerin, C. Miscible and Core-Sheath PS/PVME Fibers by Electrospinning. *Macromolecules* **2011**, *44*, 2838–2843.
25. Chen, M. L.; Dong, M. D.; Havelund, R.; Regina, V. R.; Meyer, R. L.; Besenbacher, F.; Kingshottt, P. Thermo-Responsive Core-Sheath Electrospun Nanofibers from Poly (*N*-isopropylacrylamide)/Polycaprolactone Blends. *Chem. Mater.* **2010**, *22*, 4214–4221.
26. He, D.; Hu, B.; Yao, Q. F.; Wang, K.; Yu, S. H. Large-Scale Synthesis of Flexible Free-Standing SERS Substrates with High Sensitivity: Electrospun PVA Nanofibers Embedded with Controlled Alignment of Silver Nanoparticles. *ACS Nano* **2009**, *3*, 3993–4002.
27. Uyar, T.; Havelund, R.; Hacaloglu, J.; Besenbacher, F.; Kingshott, P. Functional Electrospun Polystyrene Nanofibers Incorporating α-, β-, and γ-Cyclodextrins: Comparison of Molecular Filter Performance. *ACS Nano* **2010**, *4*, 5121–5130.
28. Chen, M.; Gao, S.; Dong, M.; Song, J.; Yang, C.; Howard, K. A.; Kjems, J.; Besenbacher, F. Chitosan/siRNA Nanoparticles Encapsulated in PLGA Nanofibers for siRNA Delivery. *ACS Nano* **2012**, *6*, 4835–4844.
29. Ma, M. L.; Hill, R. M.; Lowery, J. L.; Fridrikh, S. V.; Rutledge, G. C. Electrospun Poly(styrene-block-dimethylsiloxane) Block Copolymer Fibers Exhibiting Superhydrophobicity. *Langmuir* **2005**, *21*, 5549–5554.
30. Kalra, V.; Kakad, P. A.; Mendez, S.; Ivannikov, T.; Kamperman, M.; Joo, Y. L. Self-Assembled Structures in Electrospun Poly(styrene-*block*-isoprene) Fibers. *Macromolecules* **2006**, *39*, 5453–5457.
31. Kuo, C. C.; Lin, C. H.; Tzeng, P.; Chen, W. C. Morphology and Photophysical Properties of Luminescent Electrospun Fibers Prepared from Diblock and Triblock Polyfluorene-*block*-Poly(2-vinylpyridine)/PEO Blends. *J. Polym. Res.* **2011**, *18*, 1091–1100.
32. Wei, M.; Lee, J.; Kang, B. W.; Mead, J. Preparation of Core-Sheath Nanofibers from Conducting Polymer Blends. *Macromol. Rapid Commun.* **2005**, *26*, 1127–1132.
33. Haining, N.; Xiwang, L.; Jingqing, L.; Yunhui, Z.; Ci, Z.; Xiaoyan, Y. Formation of Core/Shell Ultrafine Fibers of PVDF/PC by Electrospinning *via* Introduction of PMMA or BTEAC. *Polymer* **2009**, *50*, 6340–6349.

34. Bhattarai, N.; Il Cha, D.; Bhattarai, S. R.; Khil, M. S.; Kim, H. Y. Biodegradable Electrospun Mat: Novel Block Copolymer of Poly(*p*-dioxanone-*co*-L-lactide)-*block*-poly(ethylene glycol). *J. Polym. Sci., Part B: Polym. Phys.* **2003**, *41*, 1955–1964.
35. Fu, G. D.; Lei, J. Y.; Yao, C.; Li, X. S.; Yao, F.; Nie, S. Z.; Kang, E. T.; Neoh, K. G. Core-Sheath Nanofibers from Combined Atom Transfer Radical Polymerization and Electrospinning. *Macromolecules* **2008**, *41*, 6854–6858.
36. Hou, H. Q.; Jun, Z.; Reuning, A.; Schaper, A.; Wendorff, J. H.; Greiner, A. Poly(*p*-xylylene) Nanotubes by Coating and Removal of Ultrathin Polymer Template Fibers. *Macromolecules* **2002**, *35*, 2429–2431.
37. Bognitzki, M.; Hou, H. Q.; Ishaque, M.; Frese, T.; Hellwig, M.; Schwarte, C.; Schaper, A.; Wendorff, J. H.; Greiner, A. Polymer, Metal, and Hybrid Nano- and Mesotubes by Coating Degradable Polymer Template Fibers (TUFT process). *Adv. Mater.* **2000**, *12*, 637–640.
38. Nair, S.; Hsiao, E.; Kim, S. H. Fabrication of Electrically-Conducting Nonwoven Porous Mats of Polystyrene-Polypyrrole Core-Shell Nanofibers *via* Electrospinning and Vapor Phase Polymerization. *J. Mater. Chem.* **2008**, *18*, 5155–5161.
39. Fong, H.; Reneker, D. H. Elastomeric Nanofibers of Styrene-Butadiene-Styrene Triblock Copolymer. *J. Polym. Sci., Part. B: Polym. Phys.* **1999**, *37*, 3488–3493.
40. He, W. N.; Xu, J. T. Crystallization Assisted Self-Assembly of Semicrystalline Block Copolymers. *Prog. Polym. Sci.* **2012**, *37*, 1350–1400.
41. Rupar, P. A.; Chabanne, L.; Winnik, M. A.; Manners, I. Non-Centrosymmetric Cylindrical Micelles by Unidirectional Growth. *Science* **2012**, *337*, 559–562.
42. Chen, S. C.; Wu, G.; Shi, J.; Wang, Y. Z. Novel "Star Anise"-Like Nano Aggregate Prepared by Self-assembling of Preformed Microcrystals from Branched Crystalline-Coil Alternating Multi-Block Copolymer. *Chem. Commun.* **2011**, *47*, 4198–4200.
43. Chen, S. C.; Li, L. L.; Wang, H.; Wu, G.; Wang, Y. Z. Synthesis and Micellization of Amphiphilic Multi-Branched Poly(*p*-dioxanone)-*block*-poly(ethylene glycol). *Polym. Chem.* **2012**, *3*, 1231–1238.
44. Wu, G.; Chen, S. C.; Wang, X. L.; Yang, K. K.; Wang, Y. Z. Dynamic Origin and Thermally Induced Evolution of New Self-Assembled Aggregates from An Amphiphilic Comb-like Graft Copolymer: A Multiscale and Multimorphological Procedure. *Chem.—Eur. J.* **2012**, *18*, 12237–12241.
45. Huang, H. Y.; Hoogenboom, R.; Leenen, M. A. M.; Guillet, P.; Jonas, A. M.; Schubert, U. S.; Gohy, J. F. Solvent-Induced Morphological Transition in Core-Cross-Linked Block Copolymer Micelles. *J. Am. Chem. Soc.* **2006**, *128*, 3784–3788.
46. Li, J. B.; Zhang, J. K.; Liu, P.; Liang, J.; Feng, S. X. Polyion Micelles with Diphase-Segregated Core: Electrostatic Self-Assembly of Poly(ethylene glycol)-*block*-poly(4-vinylpyridium) and Tetrakis (4-sulfonatophenyl) Porphyrin in Solution. *Colloid Polym. Sci.* **2011**, *289*, 193–198.
47. Tiwari, S. K.; Venkatraman, S. S. Importance of Viscosity Parameters in Electrospinning: Of Monolithic and Core-Shell Fibers. *Mater. Sci. Eng., C* **2012**, *32*, 1037–1042.
48. Kong, L. Y.; Ziegler, G. R. Role of Molecular Entanglements in Starch Fiber Formation by Electrospinning. *Biomacromolecules* **2012**, *13*, 2247–2253.
49. Chisca, S.; Barzic, A. I.; Sava, I.; Olaru, N.; Bruma, M. Morphological and Rheological Insights on Polyimide Chain Entanglements for Electrospinning Produced Fibers. *J. Phys. Chem. B.* **2012**, *116*, 9082–9088.
50. Tan, Y. Q.; Song, Y. H.; Zheng, Q. Hydrogen Bonding-Driven Rheological Modulation of Chemically Reduced Graphene Oxide/Poly(vinyl alcohol) Suspensions and Its Application in Electrospinning. *Nanoscale* **2012**, *4*, 6997–7005.
51. Mendoza, C. I. Model for the Shear Viscosity of Suspensions of Star Polymers and Other Soft Particles. *Macromol. Chem. Phys.* **2013**, *214*, 599–604.
52. Raghavan, S. R.; Riley, M. W.; Fedkiw, P. S.; Khan, S. A. Composite Polymer Electrolytes Based on Poly(ethylene glycol) and Hydrophobic Fumed Silica: Dynamic Rheology and Microstructure. *Chem. Mater.* **1998**, *10*, 244–251.
53. Massey, J.; Power, K. N.; Manners, I.; Winnik, M. A. Self-Assembly of a Novel Organometallic-Inorganic Block Copolymer in Solution and the Solid State: Nonintrusive Observation of Novel Wormlike Poly(ferrocenyldimethylsilane)-*b*-Poly(dimethylsiloxane) Micelles. *J. Am. Chem. Soc.* **1998**, *120*, 9533–9540.
54. Sayed, S. Y.; Buriak, J. M. Epitaxial Growth of Nanostructured Gold Films on Germanium *via* Galvanic Displacement. *ACS Appl. Mater. Interfaces* **2010**, *2*, 3515–3524.
55. Nagamatsu, S.; Misaki, M.; Chikamatsu, M.; Kimura, T.; Yoshida, Y.; Azumi, R.; Tanigaki, N.; Yase, K. Crystal Structure of Friction-Transferred Poly(2,5-dioctyloxy-1,4-phenylenevinylene). *J. Phys. Chem. B* **2007**, *111*, 4349–4354.
56. Wu, C. C.; Wuu, D. S.; Lin, P. R.; Chen, T. N.; Horng, R. H. Three-Step Growth of Well-Aligned ZnO Nanotube Arrays by Self-Catalyzed Metalorganic Chemical Vapor Deposition Method. *Cryst. Growth Des.* **2009**, *9*, 4555–4561.
57. Welzel, U.; Ligot, J.; Lamparter, P.; Vermeulen, A. C.; Mittemeijer, E. J. Stress Analysis of Polycrystalline Thin Films and Surface Regions by X-ray Diffraction. *J. Appl. Crystallogr.* **2005**, *38*, 1–29.
58. Lo Nigro, R.; Toro, R.; Malandrino, G.; Fragala, I. L. Hetero-epitaxial Growth of Nanostructured Cerium Dioxide Thin Films by MOCVD on A (001) TiO_2 Substrate. *Chem. Mater.* **2003**, *15*, 1434–1440.
59. Ekins-Daukes, N. J.; Kawaguchi, K.; Zhang, J. Strain-Balanced Criteria for Multiple Quantum Well Structures and Its Signature in X-ray Rocking Curves. *Cryst. Growth Des.* **2002**, *2*, 287–292.
60. Furuhashi, Y.; Nakayama, A.; Monno, T.; Kawahara, Y.; Yamane, H.; Kimura, Y.; Iwata, T. X-ray and Electron Diffraction Study of Poly(*p*-dioxanone). *Macromol. Rapid Commun.* **2004**, *25*, 1943–1947.
61. Greenfeld, I.; Arinstein, A.; Fezzaa, K.; Rafailovich, M. H.; Zussman, E. Polymer Dynamics in Semidilute Solution During Electrospinning: A Simple Model and Experimental Observations. *Phys. Rev. E* **2011**, *84*, No. 041806.
62. Greenfeld, I.; Fezzaa, K.; Rafailovich, M. H.; Zussman, E. Fast X-ray Phase-Contrast Imaging of Electrospinning Polymer Jets: Measurements of Radius, Velocity, and Concentration. *Macromolecules* **2012**, *45*, 3616–3626.
63. Casper, C. L.; Stephens, J. S.; Tassi, N. G.; Chase, D. B.; Rabolt, J. F. Controlling Surface Morphology of Electrospun Polystyrene Fibers: Effect of Humidity and Molecular Weight in The Electrospinning Process. *Macromolecules* **2004**, *37*, 573–578.